University of Nebraska - Lincoln
DigitalCommons@University of Nebraska - Lincoln

Papers in the Earth and Atmospheric Sciences | Earth and Atmospheric Sciences, Department of

2015

A fast Visible Infrared Imaging Radiometer Suite simulator for cloudy atmospheres

Chao Liu
Texas A&M University

Ping Yang
Texas A&M University, pyang@tamu.edu

Shaima L. Nasiri
Texas A&M University

Steven Platnick
NASA Goddard Space Flight Center

Kerry G. Meyer
Universities Space Research Association

See next page for additional authors

Follow this and additional works at: http://digitalcommons.unl.edu/geosciencefacpub

 Part of the Earth Sciences Commons

Liu, Chao; Yang, Ping; Nasiri, Shaima L.; Platnick, Steven; Meyer, Kerry G.; Wang, Chenxi; and Ding, Shouguo, "A fast Visible Infrared Imaging Radiometer Suite simulator for cloudy atmospheres" (2015). *Papers in the Earth and Atmospheric Sciences*. 471.
http://digitalcommons.unl.edu/geosciencefacpub/471

This Article is brought to you for free and open access by the Earth and Atmospheric Sciences, Department of at DigitalCommons@University of Nebraska - Lincoln. It has been accepted for inclusion in Papers in the Earth and Atmospheric Sciences by an authorized administrator of DigitalCommons@University of Nebraska - Lincoln.

Authors
Chao Liu, Ping Yang, Shaima L. Nasiri, Steven Platnick, Kerry G. Meyer, Chenxi Wang, and Shouguo Ding

This article is available at DigitalCommons@University of Nebraska - Lincoln: http://digitalcommons.unl.edu/geosciencefacpub/471

AGU PUBLICATIONS

JGR

Journal of Geophysical Research: Atmospheres

RESEARCH ARTICLE
10.1002/2014JD022443

Key Points:
- Correlated k distribution models for the VIIRS bands are developed
- A fast VIIRS instrument simulator is developed
- A case study is performed to validate the simulator

Correspondence to:
P. Yang,
pyang@tamu.edu

Citation:
Liu, C., P. Yang, S. L. Nasiri, S. Platnick, K. G. Meyer, C. Wang, and S. Ding (2015), A fast Visible Infrared Imaging Radiometer Suite simulator for cloudy atmospheres, *J. Geophys. Res. Atmos.*, *120*, 240–255, doi:10.1002/2014JD022443.

Received 13 AUG 2014
Accepted 1 DEC 2014
Accepted article online 3 DEC 2014
Published online 12 JAN 2015

A fast Visible Infrared Imaging Radiometer Suite simulator for cloudy atmospheres

Chao Liu[1], Ping Yang[1], Shaima L. Nasiri[1], Steven Platnick[2], Kerry G. Meyer[2,3], Chenxi Wang[4], and Shouguo Ding[5]

[1]Department of Atmospheric Sciences, Texas A&M University, College Station, Texas, USA, [2]NASA Goddard Space Flight Center, Greenbelt, Maryland, USA, [3]Goddard Earth Sciences Technology and Research, Universities Space Research Association, Columbia, Maryland, USA, [4]Earth System Science Interdisciplinary Center, University of Maryland, College Park, Maryland, USA, [5]Department of Earth and Atmospheric Sciences, University of Nebraska–Lincoln, Lincoln, Nebraska, USA

Abstract A fast instrument simulator is developed to simulate the observations made in cloudy atmospheres by the Visible Infrared Imaging Radiometer Suite (VIIRS). The correlated *k* distribution technique is used to compute the transmissivities associated with absorbing atmospheric gases. The bulk scattering properties of ice clouds are based on the ice model used for the Moderate Resolution Imaging Spectroradiometer Collection 6 ice cloud products, and those of water clouds are computed with the Lorenz-Mie theory. Two fast radiative transfer models based on precomputed ice cloud look-up tables are used for the VIIRS solar and infrared channels. The accuracy and efficiency of the fast simulator are quantified in comparison with a combination of the rigorous line-by-line (LBLRTM) and discrete ordinate radiative transfer (DISORT) models. The maximum relative errors of the simulator are less than 2% for simulated top of atmosphere reflectances at the solar channels, and the brightness temperature differences for the infrared channels are less than 0.2 K. The simulator is over 3 orders of magnitude faster than the benchmark LBLRTM + DISORT model. Furthermore, the cloudy atmosphere reflectances and brightness temperatures from the fast VIIRS simulator compare favorably with those from VIIRS observations.

1. Introduction

The Visible Infrared Imaging Radiometer Suite (VIIRS) on board the Suomi National Polar-orbiting Partnership satellite provides critical data for accurately determining cloud and aerosol properties, ocean color, sea and land surface temperatures, ice motion and temperature, fires, and Earth's albedo [*Lewis et al.*, 2010; *Lee et al.*, 2010; *Hillger et al.*, 2013]. VIIRS includes 16 moderate-resolution channels (referred to as M bands) at 0.75 km spatial resolution and 5 higher-resolution imagery channels (I bands) at 0.375 km resolution. With central wavelengths from approximately 0.4 to 12 μm, the sensor was designed to be the next generation global weather and climate imager for afternoon polar-orbiting observations. To infer cloud properties from the VIIRS observations, an accurate and efficient forward radiative transfer model (RTM) is invaluable for generating simulated reflectances or brightness temperatures for a variety of atmospheric cloud and surface conditions and can be used for retrieval error analyses and instrument calibration efforts.

Many rigorous radiative transfer schemes, such as the line-by-line radiative transfer model (LBLRTM) [*Clough et al.*, 1992, 2005], the adding-doubling algorithm [*Twomey et al.*, 1966; *Hovenier*, 1969; *Hansen*, 1971; *de Haan et al.*, 1987], and the discrete ordinate radiative transfer (DISORT) method [*Chandrasekhar*, 1960; *Liou*, 1973; *Stamnes et al.*, 1988; *Thomas and Stamnes*, 1999], have been developed and widely applied under different circumstances. For remote sensing problems involving hyperspectrally resolved or channel-averaged radiances, a rigorous approach is needed to independently and efficiently perform large numbers of simulations resolved spectrally for each wavelength/wave number due to the significant spectral variations exhibited by molecular absorption and, in the case of channel-averaged simulation, to conduct subsequent spectral integration. Performing hundreds or even thousands of monochromatic simulations is extremely time consuming; thus, rigorous RTMs are significantly limited in satellite remote sensing applications because of the large number of spatial and temporal observations. Developing computationally efficient RTMs for specific satellite-based instruments without loss of accuracy is critical for operational retrievals of atmospheric profiles as well as for the advancement of more sophisticated cloud or aerosol property retrievals [*Dubuisson et al.*, 1996, 2005; *Weisz et al.*, 2007; *Garnier et al.*, 2012, 2013;

©2014. American Geophysical Union. All Rights Reserved.
This document is a U.S. government work and is not subject to copyright in the United States.

Chen and Huang, 2014] and can also be useful for evaluating weather and climate models at the radiance level [*Huang et al.*, 2007].

One approach to achieve computational efficiency is to relax the accuracy constraints for each individual simulation; models using two streams [*Meador and Weaver*, 1980], low orders of scatterings [*Natraj and Spurr*, 2007], or precomputed look-up tables [*Wang et al.*, 2011] are typical examples of such approximations. These models normally keep the same number of single simulations but accelerate each individual simulation. Other approximate approaches for hyperspectral or band-average calculations, such as the correlated *k* distribution (CKD) method [*Arking and Grossman*, 1972; *Lacis and Oinas*, 1991; *Fu and Liou*, 1992; *Kratz*, 1995; *Shi et al.*, 2009], the principal component method [*Liu et al.*, 2006, 2009], and the optimal spectral sampling method [*Moncet et al.*, 2008], are designed to minimize the computational effort by reducing the number of individual radiative transfer simulations within a spectral band. Instead of considering each wave number within a band, such models conduct rigorous radiative transfer calculations at only a small number of representative monochromatic wave numbers. The two types of approaches have been applied to remote sensing, radiative transfer, and global climate models in both the solar and IR spectral regions. In this study, we combine the two approaches to maximize computational efficiency.

This study develops a fast RTM, i.e., an instrument simulator for cloudy atmospheres, and uses both of the previously described methodologies to minimize the computational time. While the emphasis here is in simulating the VIIRS solar and infrared channels, the approach can be extended to other imagers in a straightforward way. To obtain the TOA (top of atmosphere) reflectances or brightness temperatures, the atmospheric gaseous transmissivity and cloud optical properties are essential parameters for RTM and will be carefully considered in the fast model. Section 2 describes the development of the CKD models to determine gaseous transmissivity, and section 3 discusses the cloud optical properties. The fast radiative transfer models (FRTMs) for VIIRS solar and IR channels, respectively, are described in section 4. Section 5 validates the simulator and compares the simulated results with VIIRS observations, and section 6 summarizes the study.

2. Determination of Gas Transmissivity

As an approximate technique to line-by-line calculations such as those of LBLRTM [*Clough et al.*, 1992, 2005], the CKD is a highly efficient model to account for gaseous absorption and can be effectively incorporated into calculations of multiple scattering in aerosols and clouds. The CKD model replaces the integral of gas transmissivity over highly variable spectral space by a counterpart over a much smoother absorption coefficient space.

The transmissivity of a single gas at constant pressure and temperature within a small spectral interval of interest, e.g., the interval of a VIIRS channel, is defined as

$$T_{\mathrm{ch}}(u) = \frac{1}{\Delta\upsilon}\int_{\Delta\upsilon} e^{-k(\upsilon)u} d\upsilon, \tag{1}$$

where $k(v)$ is the gas spectral absorption coefficient at wave number v and u is the gas path length. To accurately obtain the transmissivity, the line-by-line calculation must be performed over a very fine wave number grid. This calculation requires significant computational time because the absorption coefficient is a highly variable function in spectral space. However, the transmissivity does not depend on the ordering of the spectral absorption lines within a given spectral interval, and thus, instead of integrating over the spectral space, equation (1) can be expressed as

$$T_{ch}(u) = \frac{1}{\Delta\upsilon}\int_{\Delta\upsilon} e^{-k(\upsilon)u} d\upsilon = \int_{k_{\min}}^{k_{\max}} e^{-ku} f(k) dk, \tag{2}$$

where $f(k)$ is the normalized probability distribution function for $k(v)$. To obtain $f(k)$, numerically, the range of the absorption $k(v)$ and the spectral interval are divided into N and M uniform subintervals, respectively, with width $\delta k = \frac{k_{\max}-k_{\min}}{N}$ and $\delta\upsilon = \frac{\Delta\upsilon}{M}$. We define $k_0 = k_{\min}$, $k_n = k_{n-1} + \delta k$, and $\upsilon_m = \upsilon_0 + (m - 0.5) \times \delta\upsilon$. Thus, the probability function $f(k)$ can be numerically represented by

$$f(k_i) = \frac{1}{\Delta\upsilon}\sum_{m=1}^{M} \frac{\delta\upsilon}{\delta k} W[k_{i-1} < k(\upsilon_m) \le k_i], \tag{3}$$

©2014. American Geophysical Union. All Rights Reserved.

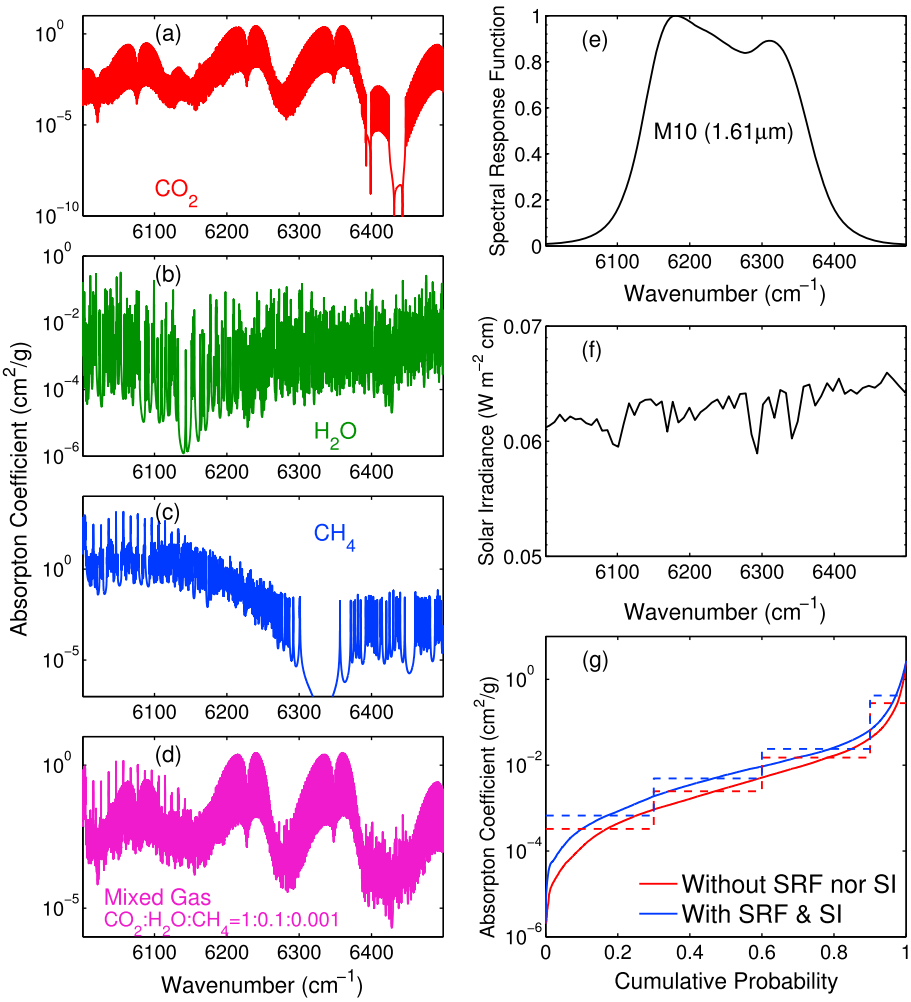

Figure 1. Example of the treatment of overlap absorption lines, spectral response function (SRF), and solar irradiance (SI) based on the CKD algorithm for the VIIRS 1.61 μm channel. (a–c) Absorption coefficient as a function of wave number for H_2O, CO_2, and CH_4.(d) Absorption coefficient for a mixed case with the ratio of the three gases being 1:0.1:0.001. (e) Spectral response function. (f) Solar irradiance at the top of atmosphere. (g) Absorption coefficient as a function of cumulative probability for the mixed gas with and without the inclusion of the spectral response function and solar irradiance.

where W is the weighting function equal to unity if its argument condition is satisfied and zero otherwise. By defining the cumulative probability function $g(k) = \int_{k_{\min}}^{k} f(k')dk'$, or in the discrete format,

$$g(k_i) = \frac{1}{\Delta\upsilon}\sum_{m=1}^{M}\delta\upsilon \times W[k(\upsilon_m) \le k_i] = \sum_{j=1}^{i} f(k_j)\delta k. \tag{4}$$

Equation (2) can be further simplified as

$$T_{ch}(u) = \int_0^1 e^{-k(g)u}dg, \tag{5}$$

where g ranges from 0 to 1 and $k(g)$ is a monotonically increasing and smooth function of g. Thus, the spectral integration in equation (5) can be evaluated with fewer points in g space between zero and unity compared to the number of wave number points required for equation (1). This approximation is known as the k distribution method and can be given by

$$T_{\mathrm{ch}}(u) = \int_0^1 e^{-k(g)u}dg = \sum_{i=1}^{N_g} e^{-k(g_i)u}\Delta g_i, \tag{6}$$

©2014. American Geophysical Union. All Rights Reserved.

where N_g is the total number of the summation points in g space. To extend the k distribution method to realistic inhomogeneous atmospheres, the CKD method assumes that the ordering of absorption lines with respect to their strengths is the same at different temperature and pressure levels, and

$$T_{ch} = \frac{1}{\Delta\upsilon}\int_{\Delta\upsilon}\exp\left\{-\int_{z_1}^{z_2}k[\upsilon, P(z), T(z)]\rho dz\right\}d\upsilon = \int_0^1\exp\left\{-\int_{z_1}^{z_2}k[g, P(z), T(z)]\rho dz\right\}dg, \tag{7}$$

where $P(z)$ and $T(z)$ are the pressure and temperature of the atmospheric layer between z_1 and z_2.

While the CKD method has been widely used, the spectral absorption coefficients associated with multiple gases have typically been treated as uncorrelated so that the standard product rule approximation could be used. *Edwards and Francis* [2000] suggested an approach to treat overlapping lines associated with different gases as a "single gas" by combining the absorption coefficients of multiple absorbing gases. The equivalent absorption coefficient for a given mixture of $(N+1)$ gases is defined as

$$K(\upsilon, R_1, R_2, \cdots, R_N) = k_0(\upsilon) + \sum_{i=1}^{N} k_i(\upsilon)R_i, \tag{8}$$

where $k_i(v)$ is the absorption coefficient of the ith gas and R_i is the density ratio of the ith gas to the reference gas, i.e., the gas with absorption coefficient of $k_0(\upsilon)$. The dominant gas can be regarded as the reference gas, and through equation (8), the absorption of $(N+1)$ gases (no more than three gases in this study) is converted into a single-gas case with an equivalent absorption coefficient $K(\upsilon, R_1, R_2, \cdots, R_N)$. This process can be repeated for a finite number of gas mixture density ratios for a fixed set of constituent gases, and a look-up table of the equivalent absorption coefficient at those fixed density ratios is precalculated. To consider any arbitrary gas density ratio associated with a realistic atmospheric profile, $K(v)$ can be found by interpolation from the tabulated k distributions.

To consider an instrument channel's (i.e., VIIRS) spectral response function (SRF, i.e., $s(v)$), the spectral transmissivity given by equation (1) is rewritten as

$$T_{ch}(u) = \frac{1}{S}\int_{\Delta\upsilon} s(\upsilon)e^{-k(\upsilon)u}d\upsilon, \tag{9}$$

where S is a normalization factor given by $S = \int_{\Delta\upsilon} s(\upsilon)d\upsilon$. To include the SRF in the CKD model, the approach suggested by *Edwards and Francis* [2000] is used, and equations (3) and (4) are modified as

$$f_s(k_i) = \frac{1}{S}\sum_{m=1}^{M}\frac{s(\upsilon_m)\delta\upsilon}{\delta k}W[k_{i-1} < k(\upsilon_m) \le k_i], \tag{10}$$

and

$$g_s(k_i) = \frac{1}{S}\sum_{m=1}^{M} s(\upsilon_m) \times \delta\upsilon \times W[k(\upsilon_m) \le k_i] = \sum_{j=1}^{i} f_s(k_j)\delta k. \tag{11}$$

In equations (10) and (11), the uniform weighting δv is changed into $s(v_m)\ \delta v$ for each spectral subinterval. TOA solar spectral irradiance variations for the solar channels can also be included in the normalization factor in a manner similar to the SRFs.

Figure 1 illustrates the treatments of overlapping absorption lines, SRF, and solar spectral irradiance for the VIIRS M10 channel centered at a wavelength of 1.61 μm. The gas spectral absorption coefficients of CO_2, H_2O, and CH_4 are plotted in Figures 1a–1c, respectively, with Figure 1d showing the effective absorption coefficient of a mixture with mass density ratios of H_2O and CH_4 to CO_2 of 0.1 and 0.001, respectively. Following equations (10) and (11), the effective coefficient of the mixture gas is weighted with the corresponding SRF (Figure 1e) and solar spectral irradiance (SI) (Figure 1f). Figure 1g shows the sorted effective absorption coefficient as a function of g; results without (solid red line) and with (solid blue line) considering the SRF and solar spectral irradiance are illustrated for comparison. In g space, the absorption coefficient becomes a smooth function, and only 4 intervals (shown by the dashed lines) at this channel are used to determine the transmissivity following equation (6). Furthermore, differences are obvious for results with and without consideration of the SRF and SI, as shown in Figure 1g.

Based on the theories and techniques described, we construct a CKD model for each of the VIIRS channels, considering only up to the three major absorptive gases. The parameters used to construct the CKD models

©2014. American Geophysical Union. All Rights Reserved.

Table 1. CKD Model Parameters for the VIIRS Channels

VIIRS Channels	Central Wavelength (μm)	Wavelength Range (μm)	Gas Considered	Number of *g* Values
M1	0.412	0.402–0.422	H_2O	4
M2	0.445	0.436–0.454	H_2O	4
M3	0.488	0.478–0.488	H_2O	16
M4	0.555	0.545–0.565	H_2O	4
M5	0.672	0.662–0.682	H_2O, O_2, O_3	8
M6	0.746	0.739–0.754	H_2O, O_2	8
M7	0.865	0.846–0.885	H_2O, O_2	8
M8	1.24	1.23–1.25	H_2O, O_2, CO_2	8
M9	1.38	1.371–1.386	H_2O	12
M10	1.61	1.58–1.64	H_2O, CO_2, CH_4	4
M11	2.25	2.23–2.28	CH_4, H_2O, N_2O	4
M12	3.70	3.61–3.79	H_2O, CH_4, O_3	4
M13	4.05	3.97–4.13	CO_2, H_2O, N_2O	16
M14	8.55	8.40–8.70	H_2O, N_2O, O_3, cont.	8
M15	10.76	10.26–11.26	H_2O, CO_2, O_3, cont.	4
M16	12.01	11.54–12.49	H_2O, CO_2, O_3, cont.	8
I1	0.64	0.60–0.68	H_2O, O_2	4
I2	0.87	0.85–0.88	H_2O, O_2	8
I3	1.61	1.58–1.64	H_2O, CO_2, CH_4	4
I4	3.74	3.55–3.93	H_2O, N_2O, CH_4	4
I5	11.45	10.50–12.40	H_2O, CO_2, O_3, cont.	16

follow the work done by *Ding et al.* [2013] for the Geostationary Operational Environmental Satellite R Advanced Baseline Imager solar channels. To build the CKD model for each of the VIIRS channels, the absorption coefficients of the gases of interest are obtained from the LBLRTM, and the molecular absorption line parameters are based on the 2008 edition of the High Resolution Transmission molecular spectroscopic database [*Rothman et al.*, 2008]. The absorption coefficients are calculated at 19 pressure levels and three temperatures (specifically, 200 K, 260 K, and 320 K) using the LBLRTM, and each set of absorption coefficients are sorted and binned following the same distribution as that of the reference pressure and temperature, chosen as 261 hPa and 260 K, respectively. Each of the VIIRS channels is divided into 4 to 16 intervals in *g* space, the number of which is determined by the gas absorption and the complexity of the overlapping gaseous absorption.

At a given g and pressure level P_0, the absorption coefficient at temperature T is given by

$$\ln[k(g,P_0,T)] = a(g,P_0) + b(g,P_0) \times (T-260) + c(g,P_0) \times (T-260)^2, \tag{12}$$

where the coefficients a, b, and c are the regression coefficients derived from absorption coefficients obtained at the three temperature values of 200 K, 260 K, and 320 K for the corresponding g values at the 19 pressure levels. In practice, the absorption coefficient at an arbitrary temperature and pressure, $k(g, P, T)$, is found first by solving equation (12), then by linear interpolation between values at the two neighboring pressures. Note that interpolation should also be performed to account for the mixing gases with special density ratios.

Table 1 lists the parameters of the CKD model for each VIIRS channel, including the central wavelength, wavelength range, absorbing gas species considered, and the number of g values. Gases considered in this study include H_2O, O_2, O_3, CO_2, CH_4, and N_2O. Up to three different absorbers are considered for each channel, and the O_3 continuum absorption (designated as "cont." in the table) is included in the IR channels by using the equations given by *Robert et al.* [1976].

The CKD is employed to produce the gaseous transmissivity of the atmosphere, and Figure 2 compares the band-averaged transmissivity and weighting profiles with results from the LBLRTM to illustrate the accuracy of the CKD results for clear-sky calculations. Results for four VIIRS channels centered at wavelengths 0.555 μm, 1.61 μm, 3.70 μm, and 10.76 μm (M4, M10, M12, and M15, respectively) are shown. In the simulations, the U.S. standard atmospheric profile is divided into 50 layers, each being 1 km thick, and the volume mixing ratios of O_2, CO_2, CH_4, and N_2O are assumed to be uniform with values of 0.21, 3.8×10^{-4}, 1.8×10^{-6}, and 3.2×10^{-7}, respectively. From left to right in Figure 2, the three columns correspond to the transmissivity in each layer,

©2014. American Geophysical Union. All Rights Reserved.

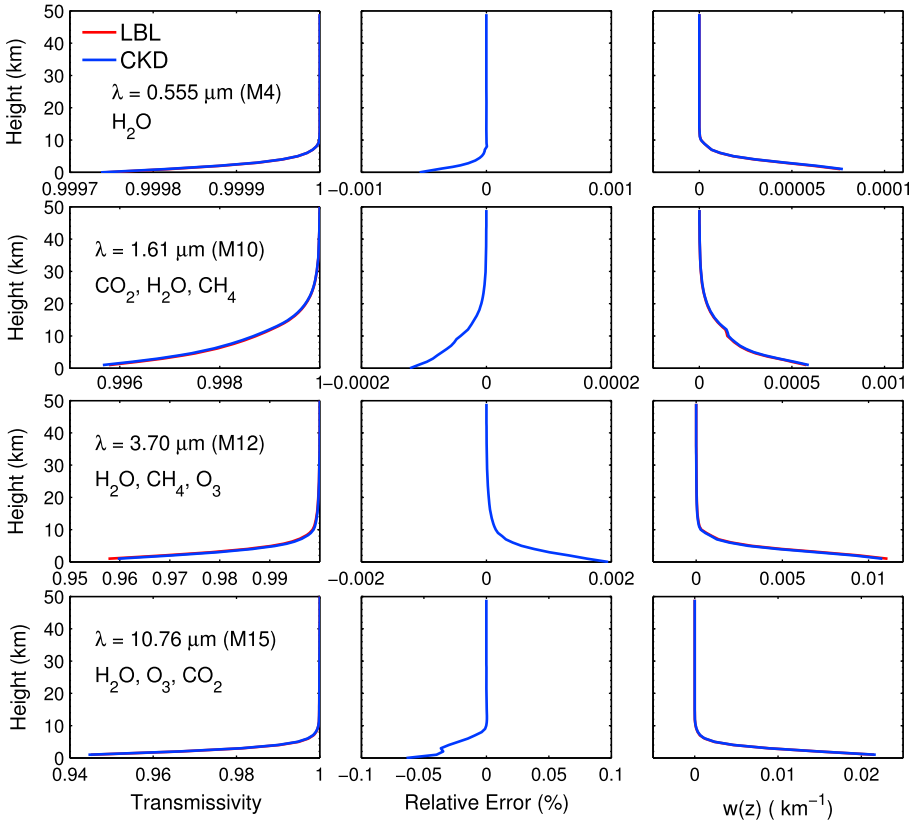

Figure 2. (left to right) Band-averaged transmissivities calculated from the LBLRTM and CKD models for VIIRS 0.555, 1.61, 3.70, and 10.76-μm channels. The U.S. standard atmospheric profile is used in the calculations.

relative transmissivity error, and weighting function profiles of the CKD models. Figure 2 indicates that the relative errors in transmissivity are less than 0.1% for the four VIIRS channels, and similar or better accuracy is also achieved for other VIIRS channels. The gas transmissivity given by the CKD model will be used to simulate reflectance and brightness temperatures under cloudy conditions.

3. Determination of Cloud Optical Properties

For cloudy sky applications, channel-averaged cloud bulk-scattering properties, for both liquid and ice phases, are required to determine the absorption, scattering, and emission of cloud layers. Here single-scattering calculations are performed at discrete sizes and wavelengths and averaged over the assumed particle size distribution and the SRF for each VIIRS channel. For the solar channels, the solar spectral irradiance is also considered. For the IR bands, the Planck function representing the thermal IR emission from an opaque cloud at 233 K is used. The details for obtaining the channel-averaged properties can be found in *Baum et al.* [2005a, 2005b].

For liquid phase clouds, the single-scattering properties are obtained using the Lorenz-Mie theory [*Mie*, 1908]. The cloud droplet size distributions are assumed to be gamma distributions [*Hansen and Travis*, 1974] with an effective variance of 0.1, and the bulk-scattering properties are calculated for effective radii ranging from 2 to 50 μm.

The particle habit (shape) model is critical in the case of ice clouds, because the microphysical and optical properties of ice clouds (particularly the optical properties in solar reflectance channels) are very sensitive to particle habits. The ice cloud model used for deriving the Moderate Resolution Imaging Spectroradiometer (MODIS) Collection 6 (C6) cloud products is applied in this study. The single-scattering properties of ice crystals are obtained from the database developed by *Yang et al.* [2013]. A combination of the discrete dipole approximation [*Yurkin and Hoekstra*, 2011] and the improved geometric optics method [*Yang and Liou*, 1996] is used to simulate the single-scattering properties of ice crystals over the entire size range. We assume the

©2014. American Geophysical Union. All Rights Reserved.

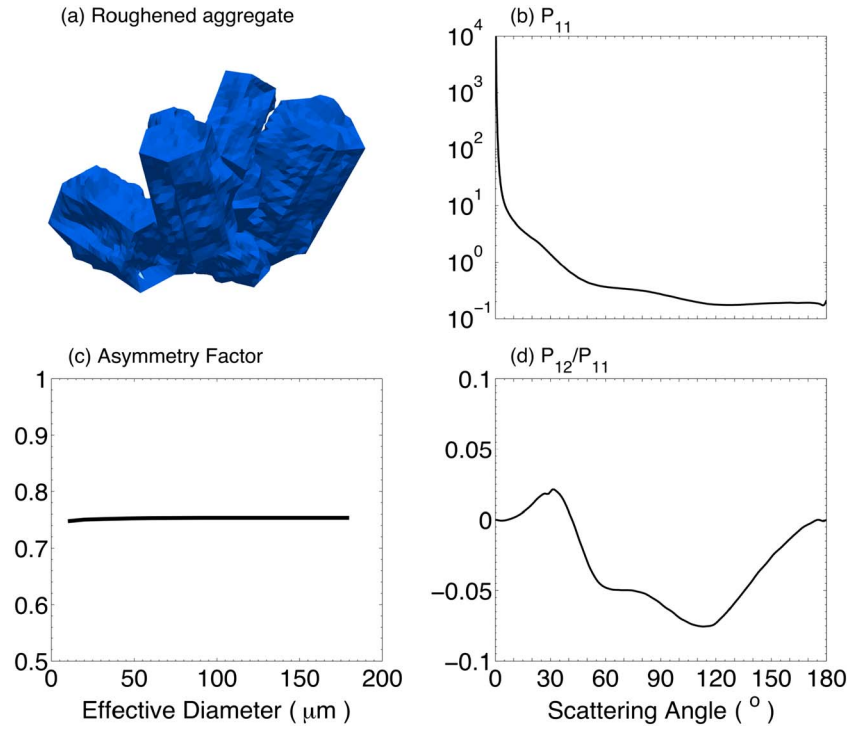

Figure 3. Geometry and scattering properties of MODIS C6 ice cloud model: (a) geometry of a hexagonal aggregate with roughened surface, (b) phase function (P_{11}) of the aggregates with an effective diameter of 50 μm at 0.65 μm, (c) asymmetry factor as a function of effective diameter at 0.65 μm, and (d) P_{12}/P_{11} element of the aggregates with an effective diameter of 50 μm at 0.65 μm.

gamma size distribution with an effective variance of 0.1 for the ice clouds, and the effective diameter ranges from 10 to 180 μm in 10 μm steps.

Figure 3 illustrates the geometry of hexagonal aggregates and their scattering properties at a visible wavelength of 0.65 μm. The hexagonal aggregate used in the MODIS Collection 6 ice model, shown in Figure 3a, is composed of eight-column elements with roughened surfaces. Figure 3c shows the asymmetry factor as a function of particle effective diameter, and Figures 3b and 3d illustrate the phase matrix elements P_{11} and P_{12}/P_{11} for an effective diameter of 50 μm. It can be seen from Figure 3b that the severely roughened surface of the C6 model results in relatively smooth phase matrix elements. Furthermore, Figure 3c indicates that the asymmetry factor of the C6 model at 0.65 μm is almost constant with a value of approximately 0.76. *Baum et al.* [2014] demonstrated that an ice habit model based on an aggregate geometry, which is composed of eight severely roughened solid hexagonal columns, provides excellent spectral consistency between the optical thicknesses inferred with a solar band technique [*Nakajima and King*, 1990] and an IR band technique [*Inoue*, 1985; *Heidinger and Pavolonis*, 2009] and leads to close agreement between the polarization properties from simulations and observations made by POLDER [*Deschamps et al.*, 1994] aboard the PARASOL.

4. VIIRS Simulator

This study considers both the VIIRS solar and infrared channels. For solar channels, cloud multiple scattering plays a much more significant role than the gaseous absorption and emission, because absorption is relatively weak at most VIIRS solar channels (except the M9 channel with strong water vapor absorption), and emissions at these wavelengths are negligible. However, gaseous absorption and emission become as important as cloud and aerosol effects (scattering, absorption, and emission) in the infrared channels. Thus, the VIIRS solar and infrared channels use different fast radiative transfer models (FRTMs).

The FRTM developed by *Wang et al.* [2013] is chosen to calculate visible through shortwave infrared spectral reflectance. This FRTM uses six independent radiative transfer equations to approximate the full radiative

©2014. American Geophysical Union. All Rights Reserved.

transfer processes for a combination of cloud, aerosol, or molecular layers; the adding-doubling algorithm implemented on a twisted icosahedral mesh is incorporated to account for overlapped cloud/aerosol layers. To further improve the FRTM efficiency, the bidirectional reflectance and transmittance distribution functions of cloud layers with different optical thicknesses and effective particle sizes are precalculated using the 128-stream DISORT, and the optical properties of water and ice clouds, discussed in the previous section, are included. Generally, the FRTM is approximately 2 orders of magnitude faster than the 128-stream DISORT and obtains TOA reflectance with relative errors normally less than 5%.

For the infrared channels, the simulator uses the FRTM developed by *Wang et al.* [2011] and *Wang et al.* [2014] to obtain the TOA brightness temperature. Similar to the FRTM used for the solar channels, the effects of cloud layers are efficiently considered by precalculated look-up tables at various optical thicknesses and effective particle sizes, which include the reflectance, transmittance, emissivity, and effective temperature. The CKD model discussed in section 2 is used to account for atmospheric gas absorption. The TOA brightness temperature differences (BTDs) given by the fast model and the rigorous DISORT are less than 0.15 K. Furthermore, the FRTM is more than 3 orders of magnitude faster than the corresponding DISORT implementation with 32 streams.

The most current DISORT code (DISORT 2.0 beta) is used to calculate the look-up tables for both FRTMs based on the band-averaged optical properties. In DISORT, the cloud phase functions are defined in terms of their Legendre polynomial expansion coefficients, and for large ice particles, thousands of Legendre polynomial terms are needed to represent a phase function that has a strong forward peak. The number of expansion terms can be greatly reduced, however, by truncating the forward peak of the phase function. The δ-fit method [*Hu et al.*, 2000] is used here for the solar channels, such that only 128 terms are sufficient to reconstruct the phase function, significantly reducing computational time for DISORT simulations. Corresponding scaling adjustments are made to the optical thickness and single-scattering albedo to account for the truncated forward energy.

The solar and IR FRTMs are combined with the CKD method to maximize the efficiency of the simulator. For each simulation, the FRTM is performed with the transmissivity obtained under each g value, and the TOA radiance of a given channel is obtained by

$$I_{\text{ch,simulator}} = \sum_{i=1}^{M} I[T(g_i)]\Delta g_i, \tag{13}$$

where $T(g_i)$ refers to the transmissivity of the ith g value and $I[T(g_i)]$ is the corresponding TOA radiance given by the FRTM.

The accuracy and efficiency of the simulator, i.e., the model based on the combination of the CKD and FRTMs, are evaluated by comparing the simulated band-averaged reflectance or BT at the TOA with the rigorous solutions given by the DISORT. For the solar channels, DISORT is combined with the CKD model to calculate the benchmark reflectance, whereas LBLRTM is used for gas absorption at the infrared channels. The spectral resolution of the LBLRTM + DISORT simulation is chosen to be 0.1 cm^{-1} for the infrared channels, and the TOA upwelling radiances are then averaged over the spectrum considering the SRF:

$$I_{\text{ch,std}} = \frac{\int_{\Delta\upsilon} s(\upsilon) I(\upsilon) d\upsilon}{S}, \tag{14}$$

where $I(v)$ is the radiation at wave number v given by the DISORT. With the TOA radiance, obtaining the corresponding brightness temperature is straightforward.

A set of comparisons at solar channels is implemented between the fast simulator and the rigorous approach, with the relative errors of TOA reflectance as a function of the viewing zenith angle shown in Figure 4. Three VIIRS channels (M4, M10, and M11) are considered for comparison, and three solar zenith angle values (10°, 30°, and 50°) are used. Figure 4 (left column) is for an ice cloud with an optical thickness of 5, and Figure 4 (right column) is for a value of 20. For all cases, the simulator yields a maximum relative error of less than 2% with respect to the rigorous approach. The relative errors slightly increase as the solar zenith angle increases and show little dependence on the cloud optical thickness. *Wang et al.* [2013] have discussed the efficiency of the solar channel FRTM in detail, and the model is approximately 500 times faster than the 128-stream DISORT in this case with single cloud layer and Lambertian surface. Furthermore, based on

©2014. American Geophysical Union. All Rights Reserved.

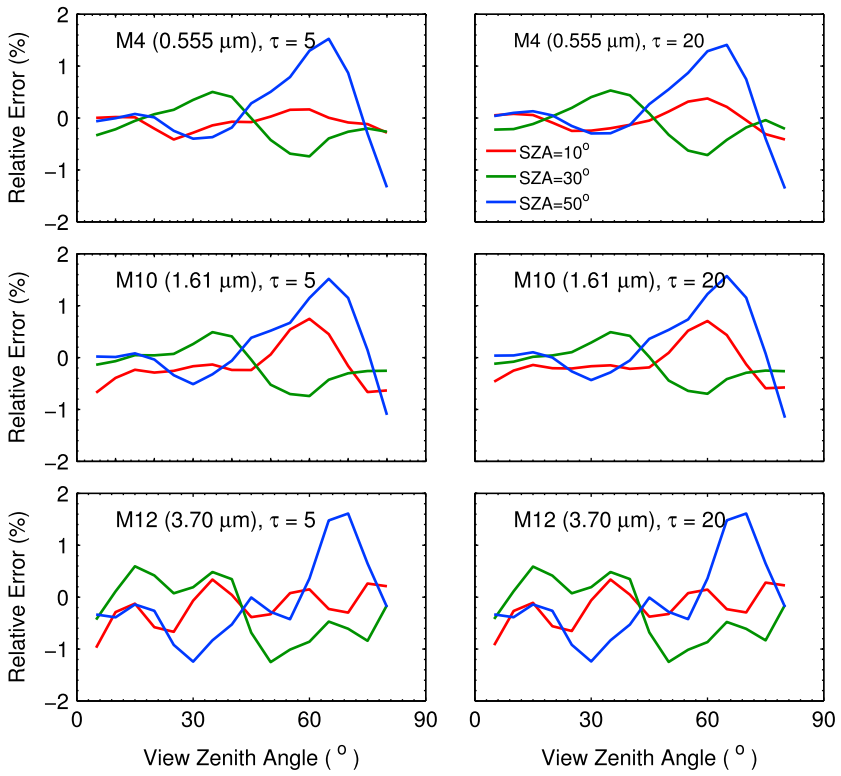

Figure 4. Relative errors of TOA reflectance at M4 (0.555 μm), M10 (1.61 μm), and M12 (3.70 μm) channels by the VIIRS simulator in comparison with the benchmark model.

the number of *g* values used in the CKD model, our simulator requires less than 16 monochromatic simulations for each channel, whereas hundreds or thousands of monochromatic simulations (at least an order of magnitude more) should be used if LBLTRM is used to consider the gas absorption. As a result, the simulator for the solar channels is approximately more than 3 orders of magnitude faster than the standard simulations based on the LBLRTM + DISORT.

To validate the simulator at the IR channels, Figure 5 illustrates the BTDs given by the simulator and the LBLRTM + DISORT at three IR channels (M14, M15, and M16). Here the BTD is defined as

$$\mathrm{BTD} = \mathrm{BT}_{\mathrm{simulator}} - \mathrm{BT}_{\mathrm{LBLRTM+DISORT}}. \quad (15)$$

Each panel of Figure 5 shows the comparison of simulation results for ice clouds based on a surface emissivity of 1 and a viewing zenith angle of 20° under different cloud conditions. The BTD is expressed as a function of optical thickness. Cloud particle effective diameters and top temperatures used for the simulations are listed in the figure. The errors in the BTDs are smaller than 0.2 K and decrease to less than 0.1 K for optically thick clouds. With a spectral resolution of 0.1 cm^{-1}, approximately 1000 monochromatic, 32-stream DISORT simulations were carried out for each VIIRS channel, and the simulator is approximately 20,000 times faster than the LBLRTM + DISORT.

It should be noted again that the simulations for both Figures 4 and 5 are based on ice clouds. For this simulator, water clouds differ from ice clouds only by their scattering properties. Our results indicate that the simulation errors for water clouds are similar to those of ice clouds and thus are not shown.

5. Comparison With VIIRS Observations

We developed a fast radiance simulator to calculate TOA reflectances or brightness temperatures of a cloudy atmosphere based on a combination of the CKD and FRTMs for the VIIRS solar and infrared channels. This section highlights a case study to assess the performance of the simulator by comparing simulated TOA reflectances and brightness temperatures with those from VIIRS observations.

©2014. American Geophysical Union. All Rights Reserved.

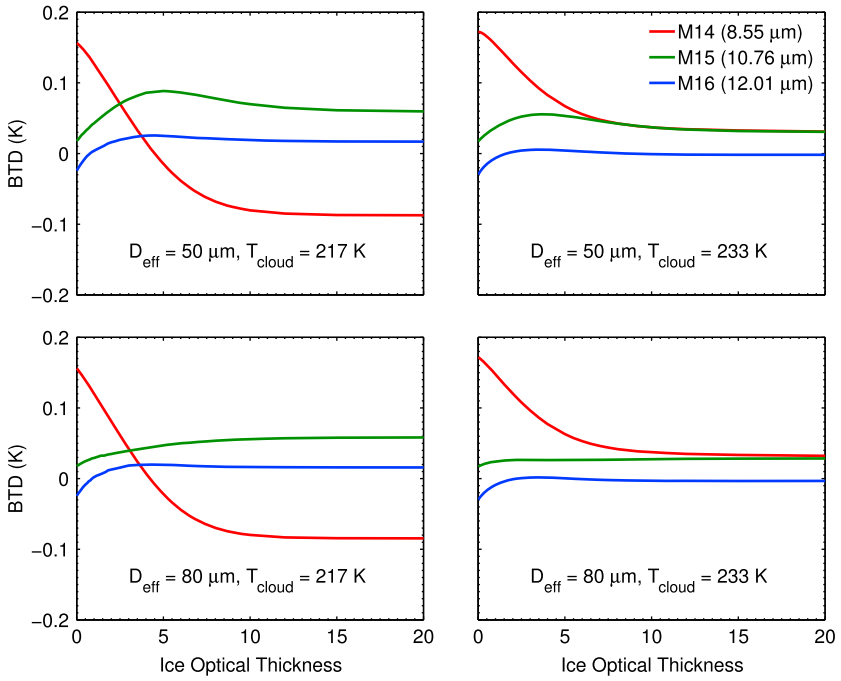

Figure 5. Brightness temperature difference (CKD + FRTM–LBL + DISORT) as a function of ice optical thickness for a viewing zenith angle of 20° at three VIIRS infrared channels (8.55, 10.76, and 12.01 μm).

As discussed in the previous sections, the forward model requires atmospheric profiles and cloud properties as input parameters. For this comparison, atmospheric profile data are obtained from the Modern Era Retrospective-Analysis for Research and Applications (MERRA) [*Rienecker et al.*, 2008] instantaneous 3 h vertical atmospheric profile product (i.e., inst3_3d_asm_Cp) that provides temperature, geopotential height, water vapor, and ozone concentrations at 42 pressure levels on a 288 × 144 mesh grid with a 1.25°×1.25° resolution. The cloud property inputs required by the simulator, including cloud thermodynamic phase, top pressure, optical thickness, and effective particle size, are from the operational MODIS Collection 6 cloud products (i.e., the Aqua MODIS MYD06_L2 product), and the 1 km resolution geolocation is obtained from the MYD03 data set. In this study, we assume the physical thickness of clouds to be 1 km, and cloud base height/pressure can be inferred from the atmospheric profiles. The atmospheric profiles and cloud properties are collocated with the VIIRS observations, with VIIRS solar and sensor view geometries used as simulator inputs.

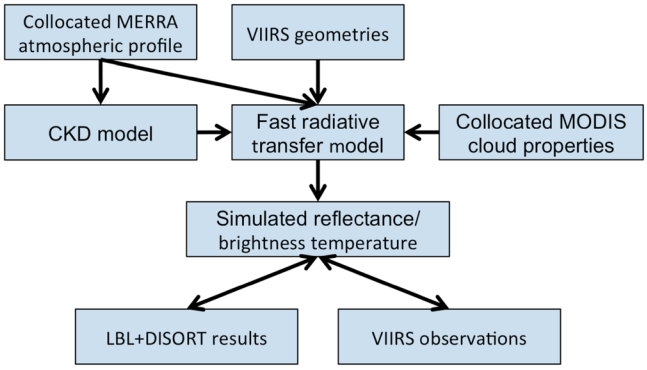

Figure 6. Flowchart outlining the fast VIIRS radiance simulator using the collocated MERRA atmospheric profile and MODIS-retrieved ice cloud thickness and effective particle size.

A schematic flowchart summarizing the fast VIIRS radiance simulator process is shown in Figure 6. The atmospheric profile is input into the CKD models to generate transmissivity of absorbing gases and provides the temperature profile for the IR simulator. The gaseous transmissivity and cloud properties are used by the FRTMs to calculate reflectances or brightness temperatures of given VIIRS solar-satellite geometries and the simulated results are compared with the corresponding VIIRS measurements to assess the performance of the simulator.

©2014. American Geophysical Union. All Rights Reserved.

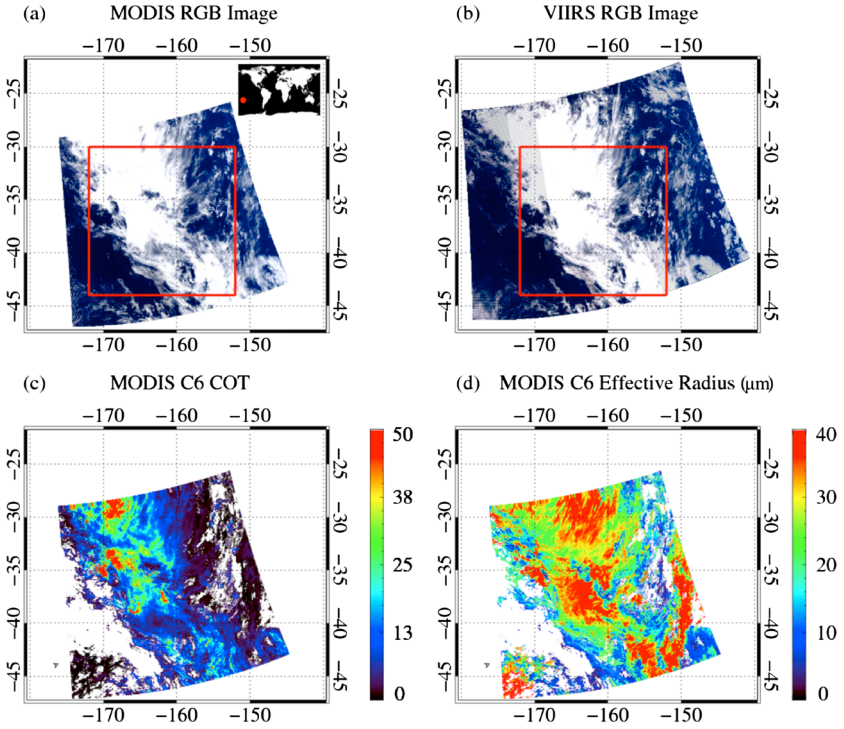

Figure 7. (a) MODIS RGB image for a granule on 3 January 2014 at 0:45 UTC taken over the South Pacific Ocean. (b) RGB image of the corresponding VIIRS granules from 00:38:47.4 to 00:41:38.2 UTC of the same day. (c and d) The MODIS Collection 6 cloud optical thickness and particle effective radius of ice clouds.

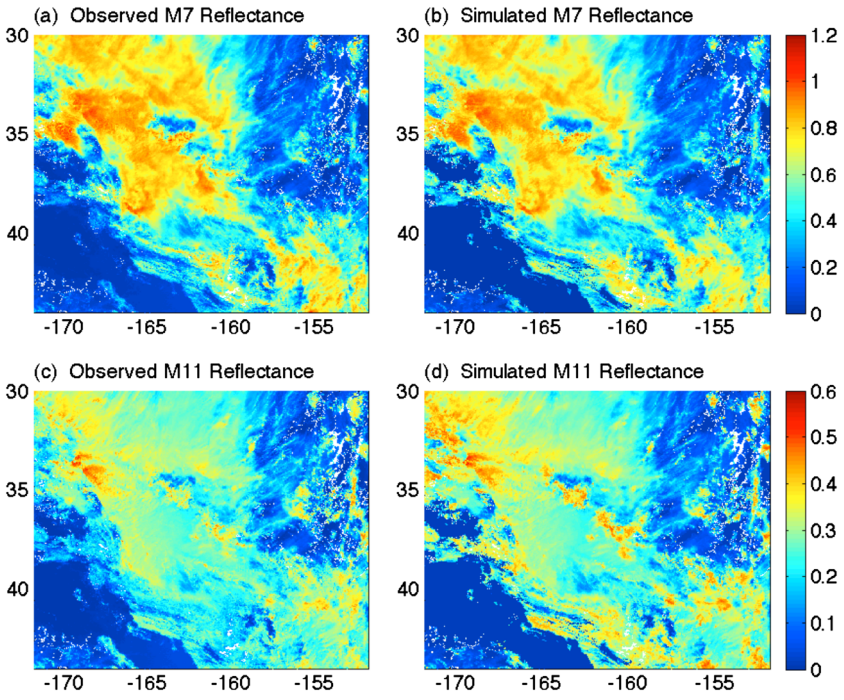

Figure 8. Comparison between the (left column) observed and (right column) simulated reflectances at the VIIRS M7 (0.865 μm) and M11 (2.25 μm) channels.

©2014. American Geophysical Union. All Rights Reserved.

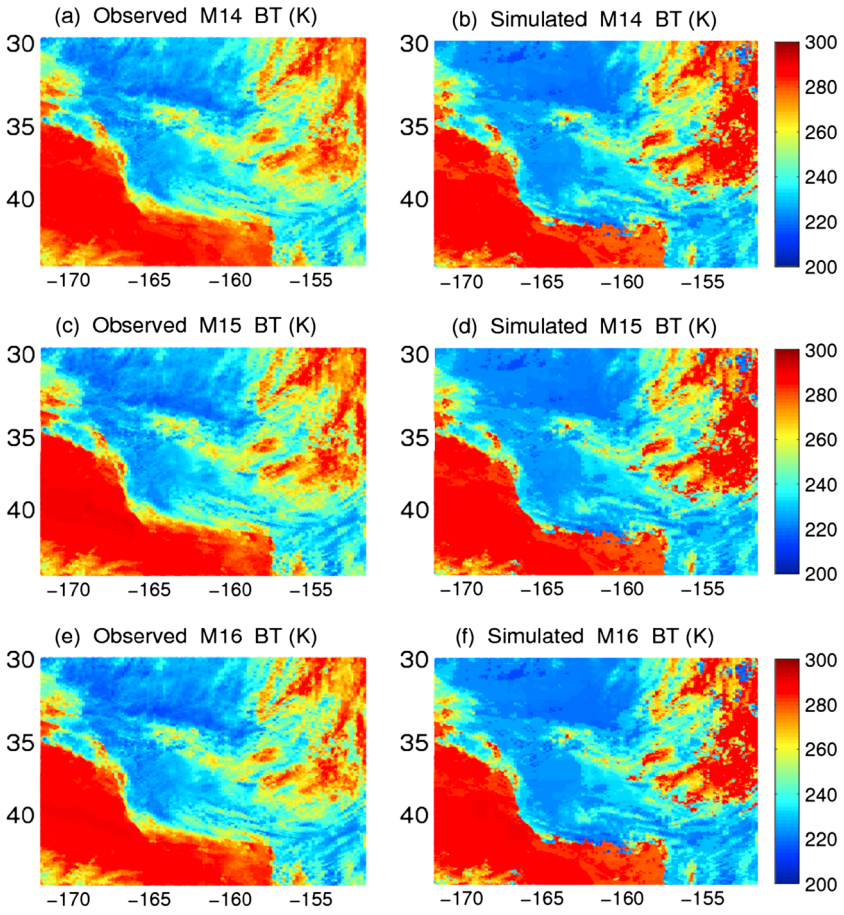

Figure 9. Comparison between the (left column) observed and (right column) simulated brightness temperatures at the VIIRS M14 (8.55 μm), M15 (10.77 μm), and M16 (12.0 μm) channels.

To avoid uncertainties associated with satellite-based cloud retrievals due to larger surface reflectances over land, only observations over ocean are considered for the present case study, specifically, the VIIRS granules taken over the South Pacific Ocean from 00:38:47.4 to 00:41:38.2 UTC on 3 January 2014. The collocated MODIS granule is taken at 00:45 UTC, approximately 4 to 6 min behind the VIIRS observations. Figure 7 shows the true color images of the MODIS (Figure 7a) and VIIRS granules (Figure 7b), with the MODIS cloud optical thickness and effective particle radius shown in Figures 7c and 7d, respectively. The red boxes in the red, green and blue (RGB) images show the region of the simulation, which is largely covered by ice clouds. In the simulation region, the cloud optical thickness ranges from a few to over 50, and the effective particle radius shows values from 5 to approximately 40 μm.

Figure 8 compares the observed (Figure 8, left column) and simulated (Figure 8, right column) reflectances at VIIRS 0.86 and 2.25 μm channels (M7 and M11). The reflectance values at the 0.86 μm channel are larger than those at the 2.25 μm channel, which is mainly due to the significant differences in the scattering properties of ice clouds at the two channels (e.g., ice clouds are much more absorptive at the 2.25 μm channel). The patterns of the reflectances given by the fast simulator are almost the same as the VIIRS observations at each channel. Furthermore, the agreement indicates the accuracy of the MOD06 products that are used as the input parameters. Note, the liquid water and ice cloud radiative models used in the FRTM were specifically chosen to match the models used in MYD06_L2 (see section 3).

Figure 9 (top to bottom) is the same as Figure 8 but for brightness temperatures at three VIIRS IR channels (i.e., 8.55, 10.76, and 12.01 μm channels (M14, M15, and M16)). The simulated brightness temperatures show close agreement with the observations. However, noticeable differences exist in the granules, and

©2014. American Geophysical Union. All Rights Reserved.

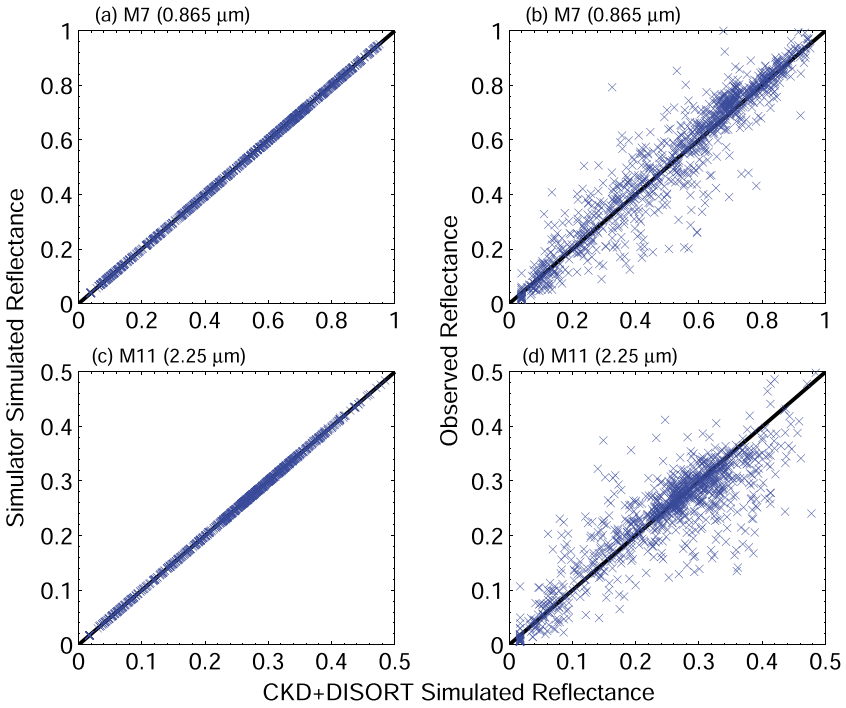

Figure 10. Comparison of the simulator (left column) simulated and (right column) observed reflectance with standard simulation based on the DISORT at the VIIRS M7 (0.865 μm) and M11 (2.25 μm) channels.

this may be due to the uncertainties in either atmospheric profiles or cloud height. The case study indicates the exceptional performance of the VIIRS simulator for both solar and IR channels.

The differences between the simulated and satellite-observed reflectances and brightness temperatures are due primarily to four sources of error: (a) error from approximations related to the fast models (i.e., the simulator itself by using the CKD and FRTMs), (b) error caused by the model assumptions (i.e., plane-parallel radiative transfer with a single cloud layer that does not consider multiple cloud layers, layer inhomogeneity, or 3-D effects [*Li et al.*, 2011; Fauchez et al., 2014]), (c) error from retrieved cloud properties (i.e., retrievals based on MODIS observations), and (d) error from atmospheric profiles (temperature, pressure, and gas concentration). Among these, only the errors from (a) can be well estimated, namely, by comparing with accurate benchmark models, as has been done in section 4. The effects related to plane-parallel RT have been discussed in several recent studies [e.g., *Li et al.*, 2011; *Fauchez et al.*, 2014] and will not be discussed here. The MODIS cloud top pressure, optical thickness, and effective particle diameter for the case study shown here were obtained approximately 4 to 6 min behind the VIIRS observations. Meanwhile, the profiles are obtained from interpolation of collocated MERRA data that have very low spatial and temporal resolutions. Thus, errors from (b), (c), and (d), which turn out to be dominant, can hardly be separated from the others or approximated independently.

To better illustrate the performance of the simulator and the relative importance of the four error factors, we randomly select 1000 pixels from the granule and use the benchmark method (DISORT; see section 4) to simulate reflectances and BTs. Figure 10 compares the reflectances (M7 and M11) given by the benchmark model (*x* axis) with those from the fast simulator (Figure 10, left column) and the VIIRS observations (Figure 10, right column). Figure 10 (left column) indicates the errors from the simulator itself, and Figure 10 (right column) illustrates the combination of the four factors. To facilitate the interpretation of the results, a 1:1 line is included in the figure. Recalling the comparison shown in section 4, the agreement between the fast simulator and the benchmark model is expected. Meanwhile, obvious differences between the observed and simulated reflectances are shown in Figure 10 (right column). The differences between Figure 10 (left and right columns) indicate that the significant errors introduced by factors other than the fast simulator itself are dominant. Figure 11 is similar to Figure 10 but for the brightness temperatures at the three infrared channels

©2014. American Geophysical Union. All Rights Reserved.

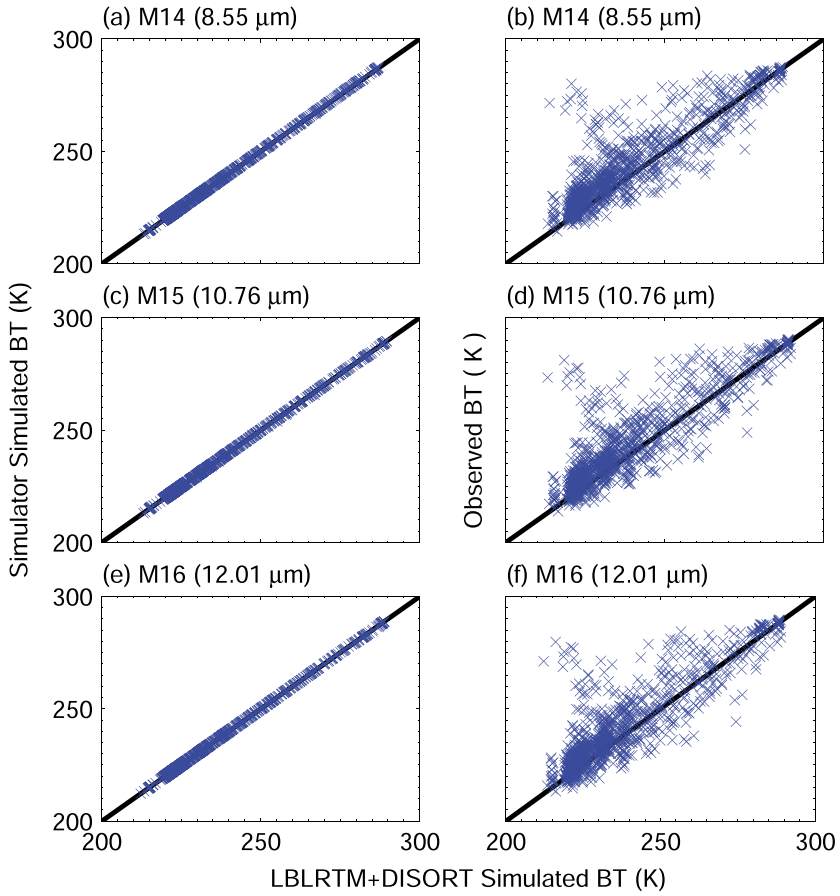

Figure 11. Comparison of the simulator (left column) simulated and (right column) observed brightness temperatures (BT) with the standard simulation based on the LBLTRM and DISORT at the VIIRS M14 (8.55 μm), M15 (10.76 μm), and M16 (12.01 μm) channels.

(i.e., M14, M15, and M16), and similar results are obtained. Figures 10 and 11 not only illustrate the accuracy of the fast simulator compared with the accurate RTM but also demonstrate that the fast simulator for both solar and infrared channels causes much smaller errors than the combined error due to the model assumption, cloud properties, and atmospheric profile.

6. Summary

This study developed a computationally efficient simulator for the VIIRS solar and IR channels in cloudy atmospheres that can be used in cloud property evaluation and retrieval. The absorption of atmospheric gases, including overlapping gas absorption, is accounted for using a VIIRS-specific CKD that considers both the spectral response function and the solar spectral irradiance. The accuracy of the transmissivity profile is estimated by comparing with the exact line-by-line results, and the relative errors in transmissivity are less than 0.1% for all VIIRS channels. Two fast RTMs are used to consider absorption, scattering, and emission of cloud layers. The channel-averaged bulk scattering properties of roughened hexagonal columns are used for ice cloud, and the properties of water cloud are given by the Lorenz-Mie theory. By comparing with the rigorous DISORT results, the relative errors for TOA reflectance at VIIRS solar channels are less than 2%, and the differences in brightness temperatures at the IR channels are less than 0.2 K. The present simulator is more computationally efficient than the standard LBLRTM + DISORT by over 3 orders of magnitude. With collocated MERRA atmospheric profiles and cloud optical thickness and effective particle diameter from the MODIS cloud product as input, the reflectances and brightness temperatures calculated by the fast simulator show close agreement with concurrent VIIRS solar and IR observations. Considering the accuracy

©2014. American Geophysical Union. All Rights Reserved.

and efficiency provided, the simulator can be used directly for cloud property retrievals related to VIIRS observations. While our fast radiative transfer model (FRTM) used in this study was applied to VIIRS channels, the FRTM can also be developed for MODIS and other satellite or airborne imagers with similar spectral coverage.

Acknowledgments

The MODIS data sets (MODIS Collection 6 MYD06_L2) used in this study are publicly available through the NASA Atmosphere Archive and Distribution System (LAADS, http://ladsweb.nascom.nasa.gov/data/). The VIIRS data sets (VIIRS Moderate Resolution Band 01–16 SDR) are available at the NOAA Comprehensive Large Array-data Stewardship System (http://www.nsof.class.noaa.gov/saa/products/search?datatype_family=VIIRS). The MERRA atmospheric profile data (inst3_3d_asm_Cp) are downloaded from the NASA Goddard Earth Sciences Data and Information Service Center (http://disc.sci.gsfc.nasa.gov/mdisc/data-holdings/merra/merra_products_nonjs.shtml). Shaima Nasiri and Ping Yang acknowledge funding support by a NASA grant (NNX11A055G). Ping Yang also acknowledges support by the endowment funds related to the David Bullock Harris Chair in Geosciences at the College of Geosciences, Texas A&M University. The computations of this study were carried out by using the Texas A&M University Supercomputing Facilities.

References

Arking, A., and K. Grossman (1972), The influence of line shape and band structure on temperatures in planetary atmospheres, *J. Atmos. Sci.*, *29*, 937–949.

Baum, B. A., A. J. Heymsfield, P. Yang, and S. T. Bedka (2005a), Bulk scattering models for the remote sensing of ice clouds. Part 1: Microphysical data and models, *J. Appl. Meteorol.*, *44*, 1885–1895.

Baum, B. A., P. Yang, A. J. Heymsfield, S. Platnick, M. D. King, and S. M. Thomas (2005b), Bulk scattering properties for the remote sensing of ice clouds II: Narrowband models, *J. Appl. Meteorol.*, *44*, 1896–1911.

Baum, B. A., P. Yang, A. J. Heymsfield, A. Bansemer, B. H. Cole, A. Merrelli, C. Schmitt, and C. Wang (2014), Ice cloud single-scattering property models with the full phase matrix at wavelengths from 0.2 to 100 μm, *J. Quant. Spectrosc. Radiat. Transfer*, *146*, 123–139.

Chandrasekhar, S. (1960), *Radiative Transfer*, Dover, New York.

Chen, X., and X. Huang (2014), Usage of differential absorption method in the thermal IR: A case study of quick estimate of clear-sky column water vapor, *J. Quant. Spectrosc. Radiat. Transfer*, *140*, 99–106.

Clough, S. A., M. J. Iacono, and J. L. Moncet (1992), Line-by-line calculation of atmospheric fluxes and cooling rates: Application to water vapor, *J. Geophys. Res.*, *97*(D14), 15,761–15,785, doi:10.1029/92JD01419.

Clough, S. A., M. W. Shephard, E. J. Mlawer, J. S. Delamere, M. J. Iacono, K. Cady-Pereira, S. Boukabara, and P. D. Brown (2005), Atmospheric radiative transfer modeling: A summary of the AER codes, Short Communication, *J. Quant. Spectrosc. Radiat. Transfer*, *91*, 233–244.

de Haan, J. H., P. B. Bosma, and J. W. Hovenier (1987), The adding method for multiple scattering of polarized light, *Astron. Astrophys.*, *183*, 371–391.

Deschamps, P., F. M. Breon, M. Leroy, A. Podaire, A. Bricaud, J. C. Buriez, and G. Seze (1994), The POLDER mission: Instrument characteristics and scientific objectives, *IEEE Trans. Geosci, Remote Sens.*, *32*, 598–615.

Ding, S., P. Yang, B. A. Baum, A. Heidinger, and T. Greenwald (2013), Development of a GOES-R advanced baseline imager solar channel radiance simulator for ice cloud, *J. Appl. Meteorol. Climatol.*, *52*, 872–888.

Dubuisson, P., J. C. Buriez, and Y. Fouquart (1996), High spectral resolution solar radiative transfer in absorbing and scattering media: Application to satellite simulation, *J. Quant. Spectrosc. Radiat. Transfer*, *55*, 103–126.

Dubuisson, P., V. Giraud, O. Chomette, H. Chepfer, and J. Pelon (2005), Fast radiative transfer modeling for infrared imaging radiometry, *J. Quant. Spectrosc. Radiat. Transfer*, *95*, 201–220.

Edwards, D. P., and G. L. Francis (2000), Improvements to the correlated *k* radiative transfer method: Application to satellite infrared sounding, *J. Geophys. Res.*, *105*(D14), 18,135–18,156, doi:10.1029/2000JD900131.

Fauchez, T., C. Cornet, F. Szczap, P. Dubuisson, and T. Rosambert (2014), Impact of cirrus clouds heterogeneities on top-of-atmosphere thermal infrared radiation, *Atmos. Chem. Phys.*, *14*, 5599–5615.

Fu, Q., and K. N. Liou (1992), On the correlated *k* distribution method for radiative transfer in nonhomogeneous atmospheres, *J. Atmos. Sci.*, *49*, 2139–2156.

Garnier, A., J. Pelon, P. Dubuisson, M. Faivre, O. Chomette, N. Pascal, and D. Kratz (2012), Retrieval of cloud properties using CALIPSO Imaging Infrared Radiometer. Part I: Effective emissivity and optical depth, *J. Appl. Meteorol. Climatol.*, *51*, 1407–1425.

Garnier, A., J. Pelon, P. Dubuisson, P. Yang, M. Faivre, O. Chomette, N. Pascal, P. Lucker, and T. Murray (2013), Retrieval of cloud properties using CALIPSO Imaging Infrared Radiometer. Part II: Effective diameter and ice water path, *J. Appl. Meteorol. Climatol.*, *52*, 2582–2599.

Hansen, J. E. (1971), Multiple scattering of polarized light in planetary atmospheres. Part I: The doubling method, *J. Atmos. Sci.*, *28*, 120–125.

Hansen, J. E., and L. D. Travis (1974), Light scattering in planetary atmospheres, *Space Sci. Rev.*, *16*, 527–610.

Heidinger, A. K., and M. J. Pavolonis (2009), Gazing at cirrus clouds for 25 years through a split window. Part I: Methodology, *J. Appl. Meteorol. Climatol.*, *48*, 1100–1116.

Hillger, D., et al. (2013), First-light imagery from Suomi NPP VIIRS, *Bull. Am. Meteorol. Soc.*, *94*, 1019–1029.

Hovenier, J. W. (1969), Symmetry relationships for scattering of polarized light in a slab of randomly oriented particles, *J. Atmos. Sci.*, *26*, 488–499.

Hu, Y. X., B. Wielicki, B. Lin, G. Gibson, S. C. Tsay, K. Stamnes, and T. Wong (2000), Delta-fit: A fast and accurate treatment of particle scattering phase functions with weighted singular-value decomposition least squares fitting, *J. Quant. Spectrosc. Radiat. Transfer*, *65*, 681–690.

Huang, Y., V. Ramaswamy, X. Huang, Q. Fu, and C. Bardeen (2007), A strict test in climate moding modeling with spectrally resolved radiance: GCM simulation versus AIRS observations, *Geophys. Res. Lett.*, *34*, L24707, doi:10.1029/2007GL031409.

Inoue, T. (1985), On the temperature and effective emissivity determination of semitransparent cirrus clouds by bispectral measurements in the 10 μm window region, *J. Meteorol. Soc. Jpn.*, *63*, 88–89.

Kratz, D. P. (1995), The correlated *k* distribution technique as applied to the AVHRR channels, *J. Quant. Spectrosc. Radiat. Transfer*, *53*, 501–517.

Lacis, A. A., and V. Oinas (1991), A description of the correlated *k* distribution method for modeling nongray gaseous absorption, thermal emission, and multiple scattering in vertically inhomogeneous atmospheres, *J. Geophys. Res.*, *96*(D5), 9027–9063, doi:10.1029/90JD01945.

Lee, E. L., S. D. Miller, and F. J. Turk (2010), The NPOESS VIIRS day/night visible sensor, *Bull. Am. Meteorol. Soc.*, *87*, 191–199.

Lewis, J. M., D. W. Martin, R. M. Rabin, and H. Moosmüller (2010), Suomi: Pragmatic visionary, *Bull. Am. Meteorol. Soc.*, *91*, 559–577.

Li, J., Y. Yi, P. Minnis, J. Huang, H. Yang, Y. Ma, W. Wang, and J. K. Ayers (2011), Radiavtive effect differences between multilayered and single-layer clouds derived from CERES, CALIPSO, and CloudSat data, *J. Quant. Spectrosc. Radiat. Transfer*, *112*, 361–375.

Liou, K. N. (1973), A numerical experiment on Chandrasekhar's discrete-ordinate method for radiative transfer: Application to cloudy and hazy atmospheres, *J. Atmos. Sci.*, *30*, 1303–1326.

Liu, X., W. L. Smith, D. K. Zhou, and A. Larar (2006), Principal component-based radiative transfer model for hyperspectral sensors, *Appl. Opt.*, *45*, 201–209.

Liu, X., D. X. Zhou, A. M. Larar, W. L. Smith, P. Schluesel, S. M. Newman, J. P. Taylor, and W. Wu (2009), Retrieval of atmospheric profiles and cloud properties from IASI spectra using superchannels, *Atmos. Chem. Phys.*, *9*, 9121–9142.

©2014. American Geophysical Union. All Rights Reserved.

Meador, W. E., and W. R. Weaver (1980), Two-stream approximations to radiative transfer in planetary atmosphere: A unified description of existing methods and a new improvement, *J. Atmos. Sci.*, *37*, 630–643.
Mie, G. (1908), Beiträge zur optic trüber medien, speziell kolloidaler metallösungen, *Ann. Phys.*, *330*, 377–445.
Moncet, J. L., G. Uymin, A. E. Lipton, and H. E. Snell (2008), Infrared radiance modeling by optimal spectral sampling, *J. Atmos. Sci.*, *65*, 3917–3934.
Nakajima, T., and M. D. King (1990), Determination of the optical thickness and effective particle radius of clouds from reflected solar radiation measurements. Part I: Theory, *J. Atmos. Sci.*, *47*, 1878–1893.
Natraj, V., and R. J. Spurr (2007), A faster linearized pseudo-spherical two orders of scattering model to account for polarization in vertically inhomogeneous scattering-absorbing media, *J. Quant. Spectrosc. Radiat. Transfer*, *107*, 263–293.
Rienecker, M. M.,et al. (2008), The GEOS-5 data assimilation system—Documentation of versions 5.0.1, 5.1.0, and 5.2.0, *NASA Tech. Memo., TM-2008*, 27 pp.
Robert, E. R., J. E. A. Selby, and L. M. Biberman (1976), Infrared continuum absorption by atmospheric water vapor in the 8–12 μm window, *Appl. Opt.*, *15*, 2085–2090.
Rothman, L. S., et al. (2008), The HITRAN 2008 molecular spectroscopic database, *J. Quant. Spectrosc. Radiat. Transfer*, *110*, 533–572.
Shi, G., N. Xu, B. A. Wang, T. Dai, and J. Q. Zhao (2009), An improved treatment of overlapping absorption bands based on the correlated *k* distribution model for thermal infrared radiative transfer calculations, *J. Quant. Spectrosc. Radiat. Transfer*, *110*, 435–451.
Stamnes, K., S. C. Tsay, W. Wiscombe, and K. Jayaweera (1988), Numerically stable algorithm for discrete-ordinate-method radiative transfer in multiple scattering and emitting layered media, *Appl. Opt.*, *27*, 2502–2509.
Thomas, G. E., and K. Stamnes (1999), *Radiative Transfer in the Atmosphere and Ocean*, Cambridge Univ. Press, New York.
Twomey, S., H. Jacobowitz, and H. B. Howell (1966), Matrix methods for multiple scattering problems, *J. Atmos. Sci.*, *23*, 289–296.
Wang, C., P. Yang, B. A. Baum, S. Platnick, A. K. Heidinger, Y. Hu, and R. E. Holz (2011), Retrieval of ice cloud optical thickness and effective particle size using a fast radiative transfer model, *J. Appl. Meteorol. Climatol.*, *50*, 2283–2297.
Wang, C., P. Yang, S. L. Nasiri, S. Platnick, B. A. Baum, A. K. Heidinger, and X. Liu (2013), A fast radiative transfer model for visible through shortwave infrared spectral reflectance's in clear and cloudy atmospheres, *J. Quant. Spectrosc. Radiat. Transfer*, *116*, 122–131.
Wang, C., P. Yang, and X. Liu (2014), A high-spectral-resolution radiative transfer model for simulating multi-layered clouds and aerosols in the infrared spectral region, *J. Atmos. Sci.*, in press.
Weisz, E., J. Li, J. Li, D. K. Zhou, H.-L. Huang, M. D. Goldberg, and P. Yang (2007), Cloudy sounding and cloud-top height retrieval from AIRS alone single field-of-view radiance measurements, *Geophys. Res. Lett.*, *34*, L12802, doi: 10.1029/2007GL030219.
Yang, P., and K. N. Liou (1996), Geometric-optics-integral-equation method for light scattering by nonspherical ice crystals, *Appl. Opt.*, *35*, 6568–6584.
Yang, P., L. Bi, B. A. Baum, K. N. Liou, G. W. Kattawar, M. I. Mishchenko, and B. Cole (2013), Spectrally consistent scattering, absorption, and polarization properties of atmospheric ice crystals at wavelengths from 0.2 to 100 μm, *J. Atmos. Sci.*, *70*, 330–347.
Yurkin, M. A., and A. G. Hoekstra (2011), The discrete-dipole-approximation code ADDA: Capabilities and known limitations, *J. Quant. Spectrosc. Radiat. Transfer*, *112*, 2234–2247.

©2014. American Geophysical Union. All Rights Reserved.